Thermomechanical properties of amorphous metallic tungsten-oxygen and tungsten-oxide coatings

E. Besozzi [a], D. Dellasega [a, b], V. Russo [a], C. Conti [c], M. Passoni [a, b], M.G. Beghi [a,*]

[a] Dipartimento di Energia, Politecnico di Milano, via Ponzio 34/3, Milano I-20133, Italy
[b] Associazione EURATOM-ENEA, IFP-CNR, Via R. Cozzi 53, Milano 20125, Italy
[c] ICVBC-CNR, Via Cozzi 54, Milano 20125, Italy

HIGHLIGHTS

- Tungsten-oxygen films, 2.1<O/W<3.1: similar amorphous structures
- O/W~2.8: switch from metallic to oxide properties
- 2.6<O/W<2.95: compact films with compressive stress, similar elastic properties
- O/W>3: porous films with tensile stress, lower stiffness due to open structure
- Thermal expansion of amorphous W oxides higher than that of crystalline oxide

GRAPHICAL ABSTRACT
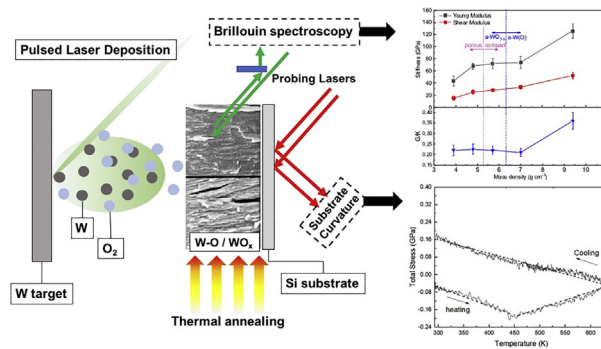
ARTICLE INFO

ABSTRACT

Metallic amorphous tungsten-oxygen and amorphous tungsten-oxide films, deposited by Pulsed Laser Deposition, are characterized. The correlation is investigated between morphology, composition, and structure, measured by various techniques, and the mechanical properties, characterized by Brillouin Spectroscopy and the substrate curvature method. The stiffness of the films is correlated to the oxygen content and the mass density. The elastic moduli decrease as the mass density decreases and the oxygen-tungsten ratio increases. A plateau region is observed around the transition between the metal-like (conductive and opaque) films and the oxide ones (non-conductive and transparent). The compressive residual stresses, moderate stiffness and high local ductility of compact amorphous tungsten-oxide films are interesting for applications involving thermal or mechanical loads. The coefficient of thermal expansion is quite high $(8.9 \cdot 10^{-6}\ K^{-1})$, being strictly correlated to the amorphous structure and stoichiometry of the films. Upon thermal treatments the coatings show a quite low relaxation temperature of 450 K. Starting from 670 K, they crystallize into the γ monoclinic phase of WO_3, the stiffness increasing by about 70%. The measured thermomechanical properties provide a guidance for the design of devices which include a tungsten based layer, in order to assure their mechanical integrity.

1. Introduction

Tungsten oxide (WO_x), of stoichiometric or nearly stoichiometric composition (2.8<O/W<3.1), and amorphous metallic tungsten-oxygen (W-O), with 2<O/W<2.8, are currently the object of several

* Corresponding author.
  E-mail address: marco.beghi@polimi.it (M.G. Beghi).

investigations, due to their interesting functional properties. In most cases these materials are in the form of supported films. Compact amorphous WO_3 films with tuned electrical and optical properties are exploited for electrochromic devices [1-3], as contact electrodes in advanced solar cells [1,4,5] and for smart windows [6]. Porous WO_3 films, due to their high active specific area, are adopted for photoelectrochemical water splitting [7,8] and photocatalysis [9,10]. W-O films, with $2 < O/W < 2.8$, have properties intermediate between those of oxides and of amorphous metals. Their color is not silvery, but dark blue; they also show an electrical resistivity in the range 1–$100\,\Omega$ cm [11]. Finally, metallic amorphous-like tungsten films [12], with $0.3 < O/W < 0.6$, can be annealed in a reducing atmosphere producing, by an alternative route, tungsten-oxide nanowires. Such nanowires show unique electric and electrochromic properties, useful for gas sensors and catalysis [13,14]. The functional properties of these films strictly depend on the specific morphology, structure and stoichiometry, and have triggered a strong characterization effort. These materials are typically exploited in the form of coatings, whose mechanical integrity is often crucial for the functional performance. In turn, the mechanical integrity basically depends on the thermo-mechanical properties. For example, compressive or tensile residual stresses affect the behavior of the films, by mitigating or favoring crack formation. Similarly, in high temperature applications, a significant mismatch between the coefficients of thermal expansion of the coating and of the substrate can induce high interface stresses, with possible coating delamination and device failure. More specifically, in an electrochromic system the W oxide film is part of a complex multilayer system: it is deposited on a transparent conductor, like ITO, and faces the electrolyte, solid or liquid, containing the ions responsible of the electrochromic effect, and can be subject to various and very different stress states [15]. Moreover, in some applications (e.g. solar-cells, thermophotovoltaic) tungsten oxide coatings operate at temperatures above room temperature [16]; this could induce phase transition or recrystallization, with a consequent variation of the as-deposited properties. Although the thermomechanical properties of tungsten based coatings can be crucial for the design of devices which exploit them, relatively fewer studies have investigated the relationship between their nanostructure, composition and mechanical properties [17-19]. The goal of this work is to achieve a more comprehensive understanding of the effects of structure, morphology and chemical composition on the thermomechanical properties of different systems of amorphous W-O and WO_x coatings, providing useful results for the design of devices. We investigate amorphous films characterized by different oxygen/tungsten ratios and morphologies. To produce them we selected the Pulsed Laser Deposition (PLD) technique, which allows a significant versatility in tailoring the structure, the morphology and the O_2 enrichment of the deposited samples [20-22]. Due to the wide variety of devices, and to the different types of substrates on which tungsten based coatings can be deposited, a single optimal set of properties cannot be identified. The compatibility of thermomechanical properties between the coating and the substrate is often more important than the absolute value for the coating alone: each application can have its own most suitable coating. Our investigation explores an interval of properties, with the aim of providing information useful to determine the most appropriate coating for each single application.

The morphology, structure and stoichiometry of the coatings are monitored by Scanning Electron Microscopy (SEM), X-Ray Diffraction (XRD), Raman spectroscopy and Energy Dispersive X-Ray Spectroscopy (EDXS). The thermomechanical characterization is performed exploiting Brillouin spectroscopy (BS) and the substrate curvature method (SC). The coupling of these two techniques has been shown to be a powerful tool for the characterization of nanostructured films, providing a broad, non-destructive characterization of the samples [23-25]. In particular, when transparent oxide coatings are investigated, BS can be able to derive, through the detection of surface and bulk acoustic waves, all the elastic moduli of the films (i.e. Young modulus(E), shear modulus (G), bulk modulus (K) and Poisson's ratio (ν)) at the same time [26,27]. SC, instead, can be exploited to measure the total stresses within the films (σ_f), the residual stresses (σ_{res}) and the coefficient of thermal expansion (CTE, or α) [25]. The thermal stability of the coatings under high temperatures is assessed by thermal annealing treatments at various temperatures up to 870 K. By performing SC measurements during the annealing treatments, it is possible to derive the evolution of σ_f in the film. The thermally induced modifications of the morphology, structure and properties are finally measured.

2. Experimental

2.1. Deposition, and characterization of morphology, composition and structure

The coatings analyzed in this work are deposited by the PLD apparatus described in detail in [20,21]. A Nd:YAG laser (pulse duration $\tau_p = 7$ ns (FWHM)), operates at its 2nd harmonic ($\lambda = 532$ m), focused on a W target (purity 99.9%); the repetition rate is 10 Hz, the laser energy ≈ 800 mJ and the laser spot about 9.2 mm^2. The fluence on target is thus ≈ 15 J cm^{-2}. W ablated species expand into a vacuum chamber (base pressure $\approx 10^{-3}$ Pa) in the presence of O_2 as background gas, with pressure varied between 5 and 60 Pa. The films are deposited onto 300 μm thick Si(100) substrates, which are double side polished for SC measurements. Morphological properties are assessed by a Zeiss Supra 40 field emission Scanning Electron Microscope (SEM), operating at an accelerating voltage of 5 kV. The composition of the samples is determined by Energy Dispersive X-ray Spectroscopy (EDXS) in the same SEM system, working with an accelerating voltage of 15 kV in order to promote the excitation of K_α and M_α electronic shells of respectively O and W. Each measurement is repeated three times at different points of the samples. XRD analysis is performed by a Panalytical X'Pert PRO X-ray diffractometer in $\theta/2\theta$ configuration, and by micro-Raman measurements, with a Renishaw InVia spectrometer equipped with an Ar$^+$ laser ($\lambda = 514.5$ nm), a 1800 g/mm grating and an edge filter with cut at 100 cm^{-1}. The laser operates at 1 mW continuum power through a 50× objective to avoid any local material modification. Finally, the mass density ρ of the deposited films is evaluated by combining weight measurements before and after the deposition using a precision balance (i.e. 10^{-4} g) and SEM cross-section for thickness determination.

2.2. Elastic moduli characterization

The elastic moduli of the coatings are evaluated by the BS spectroscopy setup described in [28], with a Nd:YAG laser (continuum operation at ≈ 200 mW, $\lambda = 532$ nm) focused on the coating surface. The scattered light is collected in the backscattering geometry without polarization analysis by a Fabry-Perot multi-pass interferometer, operating in the tandem mode, of the Sandercock type. In the case of sufficiently transparent materials light can be inelastically scattered by bulk ultrasonic waves, by the *elasto-optic mechanism* (the modulation of the refractive index by a mechanical strain). The properties of bulk waves are thus accessible [26]. At the free surface of solids Surface Acoustic Waves (SAWs) also exist, whose displacement field is confined in the vicinity of the surface, and declines with depth, the decay length being close to the wavelength. In the case of metallic samples light cannot penetrate, and interacts only with the SAWs: the process is mediated by the *surface ripple mechanism*, i.e. the dynamic corrugation of the surface due to the wave displacement. The properties of SAWs are thus accessible [23]. Since the properties of both bulk waves and SAWs depend on the mass density and the elastic properties, in both cases the elastic properties can be derived

as follows. Under the assumption of a homogeneous isotropic linear elastic medium, the elastic stiffness tensor is defined by only two independent constants, which can be taken as C_{11} and C_{44}. The other elastic moduli can be expressed in terms of these two elastic constants. Such a medium supports both longitudinal and transversal bulk waves, whose velocities v_L and v_T are respectively [27]:

$$v_L = \sqrt{\frac{C_{11}}{\rho}} \tag{1}$$

$$v_T = \sqrt{\frac{C_{44}}{\rho}} \tag{2}$$

When bulk modes can be detected, inelastic scattering of light occurs within the medium, where the optical wavevector is affected by the refractive index n of the material. The velocities v_L and v_T can be directly obtained from the frequency shifts $\Delta\omega$ of the bulk peaks in the Brillouin spectra as

$$v_{L,T} = \frac{\Delta\omega_{L,T}\lambda_0}{4\pi n}, \tag{3}$$

where λ_0 is the laser wavelength [27]. In this case C_{11} and C_{44} are obtained in a staightforward way from Eqs. (1) and (2), if both the refractive index and the mass density of the medium are known. As it will be discussed in Section 3.2, n will be estimated directly from Brillouin spectra.

Surface waves jointly depend on C_{11} and C_{44}. If only SAWs are detected, a suitable procedure must be adopted in order to derive them, which is described in detail in [23]. The spectra are recorded at different incidence angles θ, obtaining the experimental dispersion relation of the modes as function of θ. Only the component of wave vector parallel to the surface is relevant. This component depends on the incidence angle θ, but not on the refractive index. The velocities of SAWs are obtained from the frequency shifts in the spectrum, without needing the value of n, as [27]:

$$v_{SAW} = \frac{\Delta\omega_R\lambda_0}{4\pi\sin\theta} \tag{4}$$

Theoretical dispersion relations can be computed by solving the Christoffel's secular equation for an equivalent homogeneous system under the isotropic assumption. A least squares minimization can therefore be performed, between the computed dispersion relations and the measured ones. The minimization is performed with C_{11} and C_{44} as the only free parameters, for a fixed value of ρ, obtaining the most probable estimates for C_{11} and C_{44}. The number of the experimentally observed modes determines, in turn, the accuracy in the determination of the elastic properties of the films [23].

2.3. Residual stresses, CTE and annealing treatments

Residual stresses are measured by an optical implementation of the SC method. An ad-hoc developed experimental setup, fully described in [25], exploits a set of parallel laser beams to probe the curvature radius of the coating-substrate system. The scanned area is $\approx 1\,cm^2$ and the laser beams strike on the uncoated substrate surface before being collected by a high frame rate camera. Residual stresses are derived by measuring the variation of the substrate curvature before and after film deposition. According to Stoney's approximation, for a thin supported film the residual stress σ_{res} can be computed for the wafer curvature as [29]:

$$\sigma_{res} = \frac{E_s}{1 - \nu_s}\frac{t_s^2}{t_f}\frac{1}{6R_c} \tag{5}$$

where E_s and ν_s are the Young modulus and Poisson's ratio of the substrate, t_f and t_s are the thicknesses of the film and the substrate and R_c is the curvature radius of the system. In this case, R_c is measured multiple times on the same sample varying the probed position.

Tests are performed in measurement chamber, equipped with a resistive heater stage for measurements at high temperatures, temperature being measured by a thermocouple placed beneath the sample. High temperature tests are performed in vacuum (i.e. base pressure of $\approx 10^{-4}$ Pa), in order to in principle avoid any modification of the composition. The thermal stress evolution, and the CTE, are obtained by monitoring the substrate curvature change of the film-substrate system during fast heating ramps ($\approx 50\,K\,min^{-1}$), for a fixed position of the laser beams. The stress is again computed by Eq. (5); under the assumption of uniform material temperature the thermal stress can be computed as:

$$\sigma_f = \frac{E_f}{1 - \nu_f}(\alpha_f - \alpha_s)\Delta T \tag{6}$$

From Eqs. (5) and (6) the CTE of the film, α_f, can be derived, if the CTE of the substrate, α_s, and the elastic moduli of the film are known. The performances of the setup and more details on the measurements procedure can be found in [25].

Standard thermal annealing treatments are performed in the same apparatus at temperatures between room temperature (RT) and 870 K. All treatments are performed with a dwell annealing time of 1 h, and heating ramps set to $\approx 3–5\,K\,min^{-1}$. The substrate curvature, measured by R_c, is monitored during heating and cooling.

3. Results and discussion

3.1. Morphology, composition and structure of amorphous W-O and WO_x coatings

A detailed description of the growth process of these coatings by PLD can be found elsewhere [20,21]. Plane views and cross-section SEM images of the analyzed samples are shown in Fig. 1. Samples produced at O_2 pressure below 20 Pa are characterized by a compact and homogeneous structure. At 20 Pa a compact nanostructured morphology appears. At higher pressures, instead, an open porous morphology prevails. As it can be seen, at 30 Pa and 60 Pa the pressure is sufficiently high to start promoting *cauliflower* growth. These different morphologies are related to distinct growth mechanisms [20,21], strictly correlated to the expansion dynamics of the plasma plume during deposition. Low O_2 pressures promote atom-by-atom deposition, that results in the growth of compact films, while high O_2 pressures favor clusters formation inside the plume, so a porous morphology. The O/W ratio, assessed by EDXS analysis, is in turn affected by the deposition pressure. The ratios are summarized in Table 1. As it can be seen, we have O/W ≈ 2.1 at 5 Pa, increasing to ≈ 2.6 at 15 Pa. Above 20 Pa, instead, the films are almost stoichiometric WO_3. This can be associated again to an increase of interaction probability between W and O inside the plasma plume at sufficiently high O_2 pressures.

In Fig. 2 the XRD analysis of the W—O films deposited at different O_2 pressures is shown. For all the W—O films deposited in this oxygen pressure range the spectra exhibit a broad band around $26°$ with a small shoulder at about $35°$. The position of the main band is close to that of WO_3 and WO_2 crystalline peaks. None of the spectra contains peaks or bands due to α-W or β-W metallic crystals. It is worth noting that the present amorphous system is different from the amorphous-like W obtained by PLD using a He atmosphere. In that case amorphous-like W exhibits instead a broad band centered around $40°$, which is the (110) peak of α-W [12]. The formation of these two different amorphous structures related to the W—O
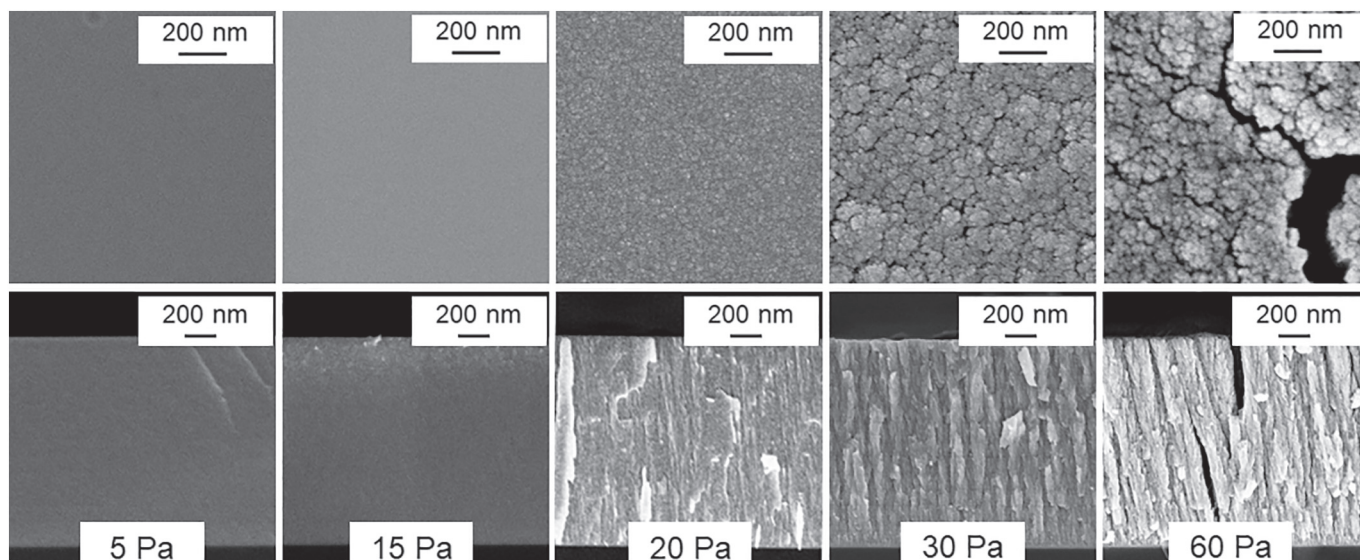
Fig. 1. SEM top view and cross-section images of tungsten oxide coatings deposited by PLD at different O_2 background pressures.

systems had been already found for magnetron sputtered deposits [18]. In particular, the films obtained at all the pressures investigated in this work have the structure which has been called 'quasi amorphous' [18].

However, a semi-quantitative resistance test discriminates the films deposited at 5 Pa and 15 Pa, which are conductors, from the films deposited at 20 Pa and above, which are insulators (resistance $>100 M\Omega$).

These findings are consistent with the outcome of Raman spectroscopy, reported in Fig. 3. All the spectra show two broad bands, a low frequency band in the range of 100–500 cm^{-1}, associated to the O—W—O bending modes, and a high frequency band in the range of 600–900 cm^{-1}, attributed to the W—O stretching modes. This band-like spectrum underlines that all the as-deposited samples are amorphous [20-22,31], although some differences regarding band shapes and intensities can be seen in the spectra. Besides the above bands, for deposition at pressure of 20 Pa or higher, the strong peak of silicon substrate at 521 cm^{-1} appears, revealing that such films are transparent oxide. On the contrary, for O_2 pressure below 20 Pa, the Raman signal is weak, and laser absorption is strong, such that the laser does not reach the Si substrate. The Raman analysis thus confirms the semiquantitative results of the electrical resistance measurements. This result is consistent with the results of Yamamoto and coworkers [11], who see an abrupt change of resistivity with varying oxygen content, consistent with the transition from silvery to dark blue films. We therefore find that the broad family of quasi-amorphous W—O films, that have very similar structures, witnessed by XRD spectra of the same type, can be subdivided in two groups. Metal-like films are conductive and opaque, while oxide films with higher oxygen content are non-conductive and transparent. It has been suggested [30] that the metal like behavior can be due to a semiconductive structure which is highly defective, such that many defect induced electronic states lie in the gap; at higher oxygen content the number of defects decreases and the band gap becomes observable. For the sake of simplicity, in the rest of this paper the metal-like tungsten-oxygen samples will be simply called metallic, or a-W(O), to underline their amorphous nature, but with a significant oxygen content. On the other hand, the transparent tungsten-oxide samples deposited at 20, 30 and 60 Pa are called a-WO_{3-x}, where $3 - x$ stands for possible stoichiometric defects. All the spectra present an additional contribution, a band at about 960 cm^{-1}, attributed in literature to the stretching mode of the W= O bonds at the surface of nanoclusters and void structures. It is thus related to material nanocrystallinity and porosity [20,31]. This band is separated from the high frequency band only in the case of optically transparent films, but unfortunately it superimposes to the second order scattering of the Si substrate. Only at 60 Pa it evolves into a better defined peak, confirming the high degree of nanostructuration and the high surface-to-volume ratio of porous a-WO_{3-x} coatings.

The mass density ρ of the samples turns out to be strictly correlated to the oxygen content. Fig. 4 shows the linear dependence of ρ on the O/W ratio. In the case of a-W(O), ρ goes from 9.4 g cm^{-3} to 7 g cm^{-3}. For a-WO_{3-x}, instead, ρ is $\approx$ 5.6 g cm^{-3} at O/W = 2.95, 4.8 g cm^{-3} at O/W = 3 and 3.9 g cm^{-3} at O/W = 3.1. In these cases, the obtained values are below the bulk value of crystalline WO_3 (7.1 g cm^{-3} [32]), remarking the higher porosity and amorphous structure that characterizes our samples. As a comparison, we reported in Fig. 4 the mass densities related to sputtered WO_x films that are commonly exploited for solar cells research and electrochromic devices [33]. As it can be seen, sputtered and PLD films having similar O/W ratios also have very similar mass densities. This is an important and somewhat surprising result since the PLD and

Table 1
O/W stoichiometric ratio, mass density, thickness, refractive index (at 532 nm), residual stress (σ_{res}) and elastic modulus (E) of the coatings.

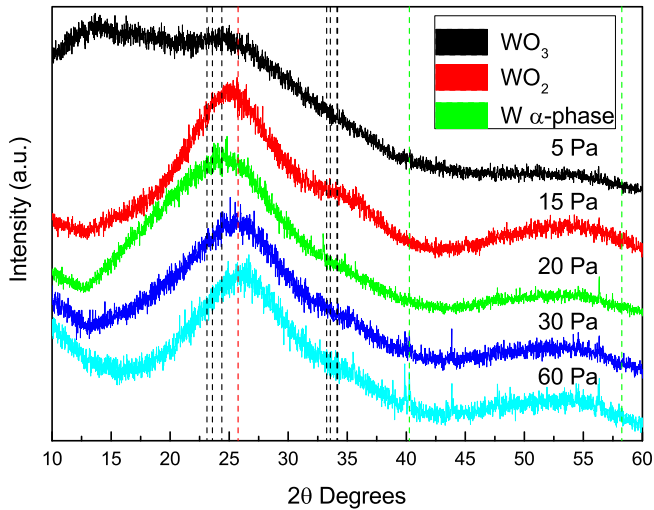| O_2 Pressure (Pa)	O/W	ρ (g cm^{-3})	Thickness (μm)	n (532 nm)	σ_{res} (MPa)	Elastic modulus (GPa)
5	2.1	9.4	3.1 ± 0.32	–	− 120 ± 50	125 ± 20
15	2.6	7	3.1 ± 0.35	–	− 85 ± 25	74 ± 10
20	2.95	5.7	3.3 ± 0.4	1.88 ± 0.1	− 50 ± 5	72 ± 8
30	$\approx$ 3	4.8	3.3 ± 0.4	1.68 ± 0.08	50 ± 7	68 ± 5
60	3.1	3.9	3.2 ± 0.35	1.49 ± 0.1	20 ± 5	43 ± 8

Fig. 2. XRD analysis of tungsten oxide coatings deposited at different O_2 background pressures. The shoulder at low angles for the 5 Pa sample is most probably an artefact due to a different sample holder.

Fig. 4. Measured mass density as function of the O/W ratio. Measured data are compared to literature values of WO_x films deposited by magnetro-sputtering [33]. The blue dotted-line separates metallic a-W(O) samples from oxide a-WO_{3-x} ones.

the sputtering processes are characterized by very different energies of the ablated particles that, in turn, could deeply affect the structure of the film and its mass density. Since it is well known that ρ, disregarding the crystalline size, has a strong influence on the thermomechanical properties of a material, one can expect similar thermomechanical properties between PLD and sputtered films of comparable O/W ratio. This would extend the results we obtain for PLD films to a more general family of tungsten-oxygen coatings, the PLD process being able to extend the range of accessible O/W ratios.

3.2. Residual stresses and elastic moduli of as-deposited coatings

The obtained results for the residual stresses σ_{res} are shown in Fig. 5 as functions of the mass density ρ. Two main regions can

be observed, which correspond to the change of film morphology: (i) compressive stresses in the case of compact samples, (ii) tensile stresses in the case of porous films. Moreover, within the compressive region σ_{res} depends on ρ, decreasing from -120 MPa in the case of metallic a-W(O) to -50 MPa for a-WO_{3-x}, with ρ ranging from 9.4 to 5.6 g cm^{-3}. On the other side, the tensile stress decreases from $\approx$ 50 MPa to 20 MPa as ρ decreases from 4.8 to 3.9 g cm^{-3}.

The observed different nature of the residual stresses can be directly associated to the PLD process, and more generally to the growth of σ_{res} in PVD coatings. In general, the magnitude and the nature of σ_{res} is associated to various contributions, namely intrinsic stresses (σ_i) and thermal stresses (σ_{th}) that arise during deposition. In the particular case of PLD at room temperature intrinsic stresses prevail over the thermal counterpart. A detailed description of the nature of σ_i can be found elsewhere [34]. For the purpose of
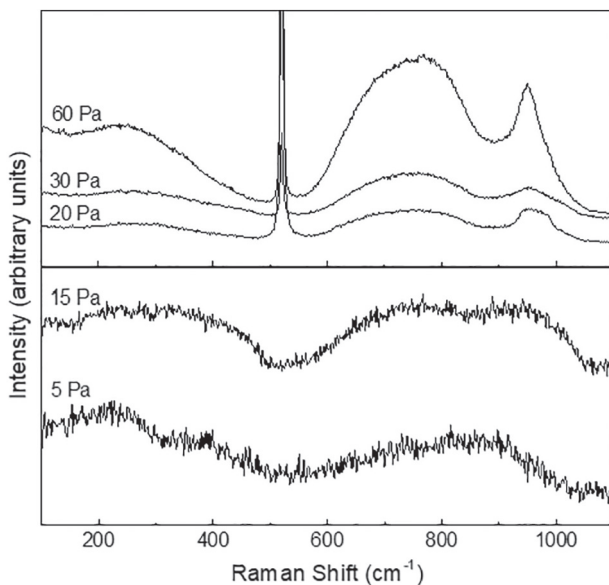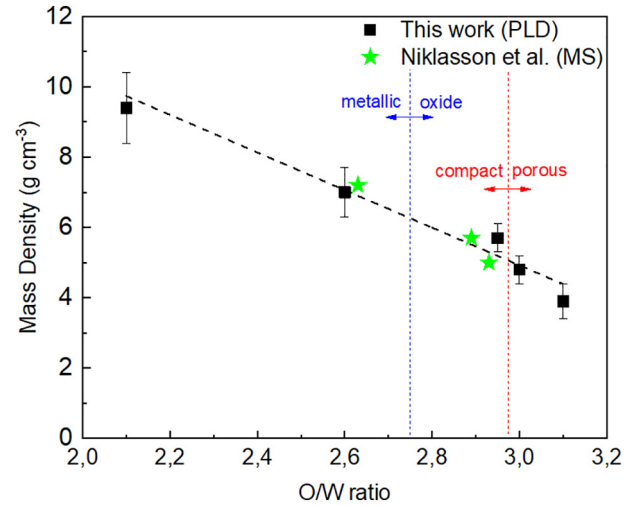

Fig. 3. Raman spectra of tungsten oxide coatings deposited at different O_2 background pressures. The Si substrate peaks are at 521 cm^{-1} and at 960 cm^{-1}.
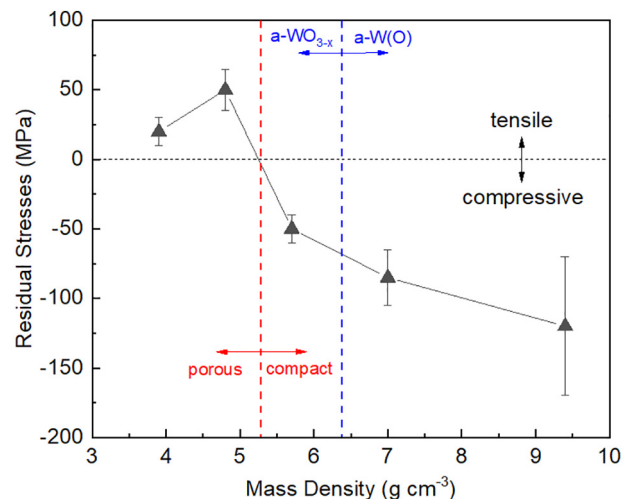

Fig. 5. Measured residual stresses as function of mass density. The red line separates compact samples from porous ones, the blue one, instead, a-W(O) from a-WO_{3-x}.

the present work, it is important to underline the fact that intrinsic stresses are determined by the sum of various contributions: (i) tensile stresses originating from the grain growth process (σ_{growth}), (ii) compressive stresses related to the adatoms diffusion to grain boundaries (σ_{diff}) and (iii) compressive stresses related to ion irradiation of the growing surface (σ_{ion}). Among them, σ_{ion} is commonly the dominant part when the energy of the ablated species is sufficiently high to promote knock-on displacements of surface adatoms (i.e. *atomic peening effect*). This leads to a consequent formation of defects and the growth of a compressive σ_i that can reach up to several GPa. In our case, the highest particles energy is found for depositions at the lowest pressures, resulting in compact high density coatings, consistently characterized by a compressive σ_{res}. When the energy decreases, σ_{ion} becomes less relevant. In the case of porous films, the existing intercolumnar voids network limits atom mobility between columns. This inhibits grain boundaries motion, such that the tensile σ_{growth} prevails on the compressive σ_{diff}. This is again in accordance with our experimental evidence in the case of porous films, where σ_{res} is tensile. This well distinct σ_{res} behavior can provide a guidance for the selection of films for various applications. Indeed, a compressive residual stress is beneficial for the mechanical behavior of the coatings, by increasing the cracks, wear and corrosion resistance. Such a resistance is particularly important for applications where high temperatures or external loads are applied. Tensile stresses, on the contrary, tend to decrease fatigue strength and life, to increase crack propagation, and to lower the resistance to environmentally assisted cracking. The higher cracking probability of tensile coatings is well highlighted by SEM images in Fig. 1, where a high density of through-thickness cracks is found at 60 Pa. The elastic moduli of the coatings are then determined by Brillouin spectroscopy. As discussed in Section 2.3, the moduli are derived under the isotropic homogeneous condition. This condition is well satisfied for compact amorphous coatings. However, tree-like nanostructure in porous samples can induce a substantial anisotropy of the mechanical properties of the films, such as the in-plane properties can differ from the out-of-plane ones. Possible anisotropy effects on the elastic moduli of nanostructured tungsten films measured by Brillouin spectroscopy have already been considered [23]. The elastic moduli reported here for porous samples, computed under the isotropic assumption, can be seen as lower bounds for the real anisotropic moduli Brillouin spectra recorded for a-W(O) and a-WO$_{3-x}$ samples are shown in Fig. 6a and b respectively. In the case of metallic a-W(O) coatings, only a low frequency mode can be detected. This mode is associated to the surface Rayleigh wave (R) of the film, the prototype of SAWs. In the case of optically transparent WO$_{3-x}$ two additional peaks become visible: the mid-frequency transverse bulk acoustic wave (T) and the high frequency longitudinal bulk acoustic wave (L). The spectra obtained at 20 and 30 Pa are quite similar, while at 60 Pa an evident shift of the modes towards lower frequencies is detected. The frequencies of these peaks depend on different factors, such as the elastic properties, mass density and the refractive index, as mentioned in Section 2.2. The observed peaks shifts can be thus attributed to a variation of all these properties. In addition, at 60 Pa the R mode disappears. This is due to the open porous morphology, that does not support surface waves propagation.

In the case of a-W(O) coatings, the thickness of the sample (i.e. ≈ 3 μ m) is such that the displacement field associated to SAWs is essentially confined within the films. The coatings thus behave like semi-infinite media, with two main consequences. On the one hand, the SAWs are not dispersive (i.e. the frequency of the modes does not depend on the wavevector, i.e. on θ), such that, in principle, the information from only one measurement at one incidence angle θ could be sufficient. On the other hand, this limits the number of possible detectable SAWs. For a-W(O) films, only the elastic information carried by the R wave can be exploited, following the procedure described in Section 2.2, thus limiting the accuracy in the estimation
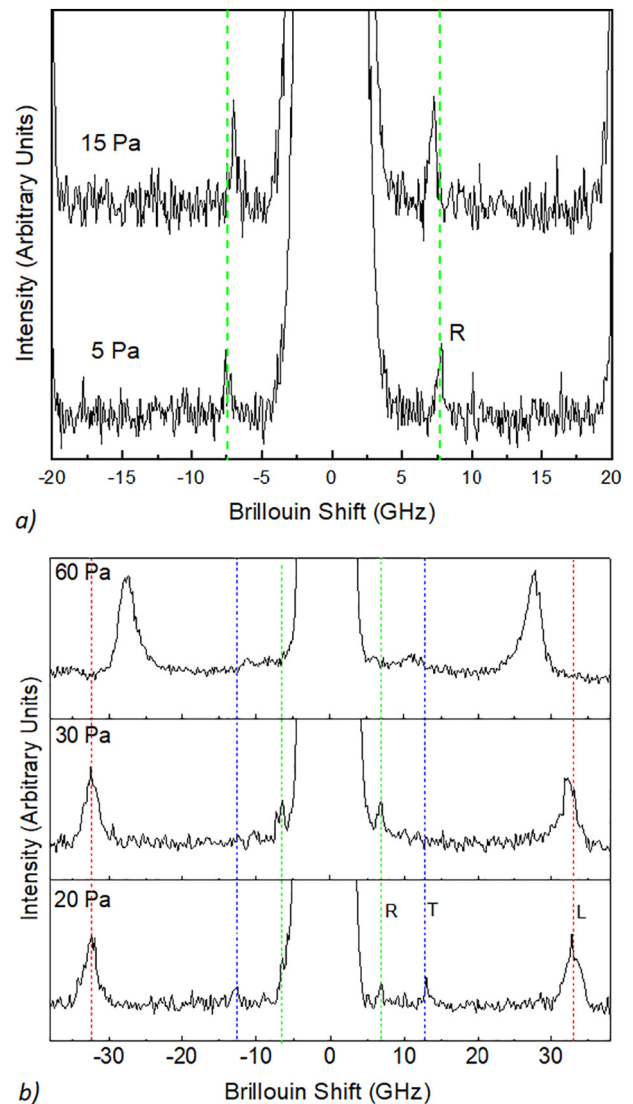

Fig. 6. Brillouin spectra recorded at an angle of incidence $\theta = 60°$. $R =$ Rayleigh mode, $T =$ transverse bulk mode, $L =$ longitudinal bulk mode. a) a-W(O) coatings, b) a-WO$_{3-x}$ coatings.

of the elastic moduli. In the case of a-WO$_{3-x}$ films, instead, the elastic moduli can be derived directly from the bulk peaks frequencies through Eqs. (1), (2) and (3). In order to do that, the refractive index of the films must be known. In this case, the simultaneous presence of the R and T waves, observed at 20 Pa and 30 Pa, is exploited to derive a consistent estimation of n. Due to its predominantly shear nature, the Rayleigh velocity v_R can be approximated in terms of v_T as $v_R \approx f(v)v_T$ [35], where $f(v) = \frac{0.862 + 1.14v}{1 + v}$, v being the Poisson's ratio of the film. In the case of W based materials, the Poisson's ratio has been found in the range between 0.28 and 0.45 [23]. With v in this range, the values of $f(v)$ remain between two close bounds: 0.933 ± 0.015, such that considering $v_T \approx 0.933 v_R$ introduces at most a 1.6% error in the approximation of n. For this reason, we compute v_R from the R peak frequency (see Fig. 6b), and then we substitute it in Eq. (3) to extract an estimation of n. This procedure is done for the samples deposited at 20 and 30 Pa, where the R and T modes are simultaneously present. At 60 Pa, the R mode is not present. Since it is reasonable to consider that the polarizability of a-WO$_{3-x}$ does not change between 20 Pa and 60 Pa (e.g. no effects related to crystallization), n can be consistently estimated by means of the well-known *Lorenz-Lortentz* correlation [36]:

$$\rho_{60} = \rho_{20}\,\frac{n_{20}^2 - 1}{n_{20}^2 + 2}\,\frac{n_{60}^2 + 1}{n_{60}^2 - 1} \qquad (7)$$

where ρ_{20} and ρ_{60} are the mass densities of the amorphous coatings at 20 and 60 Pa respectively, while n_{20} and n_{60} the corresponding refractive indexes. The obtained values of n at 532 nm are summarized in Table 1. For example, in the case of compact a-WO$_{3-x}$ we obtain a refractive index of $\approx$ 1.88 which is in good agreement with the ones reported in literature for compact amorphous WO$_3$ films (i.e. $\approx$ 1.9) [32,37].

From the estimation of n at 532 nm, C_{11}, C_{44} and all the elastic moduli are finally obtained. Fig. 7 summarizes the values of the elastic Young modulus (E), the shear modulus (G) and the shear to bulk modulus ratio (G/K), which, in particular, can be seen as an index of local ductility of the material [23]. In Fig. 7a the moduli are plotted as function of ρ, while in Fig. 7b versus the O/W ratio. As it can be seen,
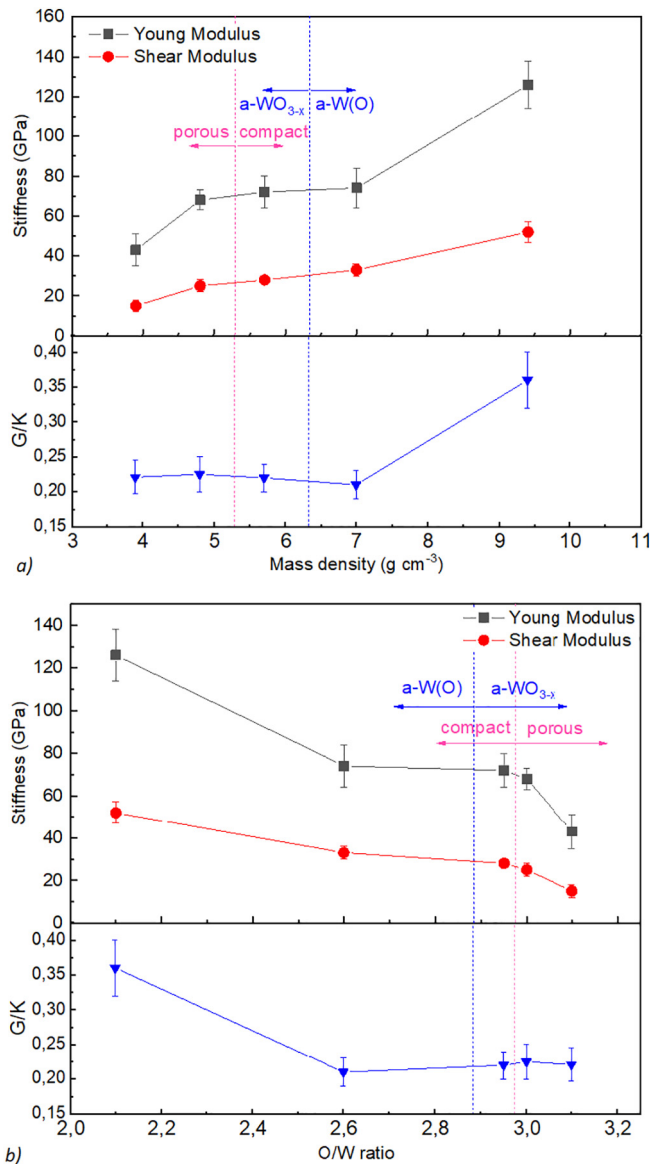
a strong dependence of the moduli on ρ and the O/W ratio is found: as ρ decreases and O/W increases the stiffness drastically decreases. Metallic a-W(O) coatings are characterized by a higher stiffness with respect to the oxide counterpart. In the metallic region E goes from $\approx$ 125 GPa to $\approx$ 74 GPa, coherently G drops from 52 GPa to 33 GPa. G/K, instead, goes from $\approx$ 0.36 to $\approx$ 0.21. This is a non-obvious trend, since from SEM and Raman analysis there is not an appreciable difference between these samples. At $\rho = 7$ g cm^{-3}, which corresponds to O/W = 2.6, a plateau of the moduli is reached: the material changes its chemical configuration, by forming tungsten-oxide, but the properties are not affected even if ρ decreases between the samples. In particular, E remains between 68 and 72 GPa, G between 25 and 28 GPa and $G/K \approx$ 0.21. This is consistent with the XRD analysis, which indicates very similar structures of these films, while resistivity and Raman measurements indicate instead a modification of the electronic states. Finally, when evident intercolumnar pores appear, E and G further drop to $E = 43$ GPa and $G = 16$ GPa, at 60 Pa, which confirms that mass density is the main parameter in determining the elastic moduli.

It is interesting to compare the stiffness observed for metallic a-W(O) films with the one proper of metallic amorphous-like W (i.e. $E = 150$ GPa, $G = 50$ GPa $\rho = 9$ g/cm^3 [23]). For an O/W ratio of 2.1 the decrease is not so important (125 GPa) considering that the a-W(O) system is determined by a different interplanar distance, compared with amorphous-like W (respectively 3.54 Å and 2.31 Å), and an amount of stored oxygen which is fivefold (2.1 compared with 0.4). Rising the oxygen content O/W from 2.1 to 2.6, the material becomes much more soft probably due to a decrease of the film density. Also the mechanical properties of a-WO$_{3-x}$ are lower in comparison with cubic WO$_3$ (i.e. $E = 258$ GPa, $G = 100$ GPa, $G/K = 0.48$ [38]). In this case, instead, the difference can be attributed to the specific amorphous structure of the film. As a result of the loss of the long range order proper of crystalline materials, the interatomic potential in the case of amorphous materials can be lowered. This, in turn, can be associated to a higher mean interatomic distance, which means a lower mean interatomic binding energy, so lower elastic moduli [39]. However, this can confer the material some peculiar properties. For example, the drop observed for G/K is related to an increase of local ductility, so to a higher ability of the material to locally allocate shear flow. In these terms, a-WO$_{3-x}$ films can be macroscopically brittle but microscopically capable of sustaining shear flow [40]. These results can be compared to the few ones reported in literature for PVD WO$_3$ coatings [17,18,41]. Parreira et al. [18] found a Young modulus of amorphous WO$_3$ films of $\approx$ 100 GPa, which is slightly higher than our values. For lower oxygen contents (i.e. O/W below 3) the discrepancy is less pronounced: they found E varying between 170 and 100 GPa for O/W ratios between 2 and 2.6, which corresponds to the E values we measured for a-W(O) coatings of 125 GPa and 74 GPa. Polcar et al. [41] and Carrejo et al. [17], instead, report higher Young modulus (i.e. between 110 and 164 GPa) for compact amorphous WO$_3$ coatings. Nevertheless, the correlation between all these results is difficult since there is no information about the material mass density, that, as already mentioned, severely affects the elastic properties of the material. However, the authors show an evident softening of the coatings with O$_2$ enrichment in the deposition atmosphere, which is in agreement with our results. The previous mechanical characterization highlighted that compact a-WO$_{3-x}$ films (deposited at 20 Pa of O) are characterized by interesting mechanical properties, such as compressive residual stresses and high local ductility, which can be fruitful for a wide range of applications. For this reason, they are chosen as the reference samples for successive characterizations. We thus characterize the CTE of as-deposited a-WO$_{3-x}$ films and the evolution of σ_f during thermal treatments, as well as we investigate the influence of different annealing temperatures on the morphology, the structure and on the elastic moduli.

Fig. 7. Elastic moduli the coatings. a) Young Modulus E, shear modulus G and G/K ratio as function of film mass density. b) The same properties as function of the stoichiometric ratio.

3.3. Coefficient of thermal expansion and stress evolution of a-WO$_{3-x}$ coatings

The *CTE* of a-WO$_{3-x}$ films is determined by the procedure described in Section 2.3. The standard thermal treatment adopted to this purpose is shown in the inset of Fig. 8; the total film stress σ_f is monitored during heating and cooling. The linear fit of the mean value of the stress (i.e. the dotted line) during the first heating steps is then exploited to derive the *CTE* of the film. From Eq. (6), the slope of the dotted line is equal to $\frac{d\sigma_f}{dT} = \frac{E}{1-\nu}(\alpha_f - \alpha_{Si})$. In this way, we obtain a mean *CTE* of $8.6 \cdot 10^{-6}$ K^{-1} between 273 and 450 K. Very little information about the CTE of tungsten-oxide is available in literature, but it is known that tungsten-oxide materials can have very different thermal expansion coefficients, that are strongly correlated with the specific stoichiometry and can even be negative at high temperatures. For example, the CTE at room temperature can vary from $1.3 \cdot 10^{-6}$ K^{-1} in the case of W$_{18}$O$_{49}$ to $3.3 \cdot 10^{-6}$ K^{-1} for WO$_2$ and between 8 and $15 \cdot 10^{-6}$ K^{-1} for WO$_3$ [42-44]. The value we find is higher than the one of the Si substrate (i.e. $2.6 \cdot 10^{-6}$ K^{-1}), which explains the negative slope of the linear fit, and is in agreement with the range of values reported in literature. Differences between literature values and our result can be attributed to a different structure of the material (e.g. crystalline vs amorphous) and possible stoichiometric defects. As it can be seen in Fig. 8, a compressive residual stress is initially developed during the heating cycle for temperatures up to 450 K. The stress magnitude increases, as expected, linearly with heating temperature up to 450 K. However, after 450 K, which corresponds to a stress of ≈ -180 MPa, the stress variation reverses its sign, the total stress eventually becoming tensile. This is a strong evidence of the beginning of some structural evolution. The tensile nature of the developed stress can be associated to the observed volume shrinkage which, in turn, relates to the beginning of diffusion and grain growth processes [34]. These processes continue until the maximum temperature is reached. Upon cooling, instead, the tensile stress associated to the coefficient of thermal expansion mismatch between the film and the substrate increases linearly with decreasing temperature. The linear trend upon cooling shows almost the same slope of the heating cycle. This slope, as already mentioned, is related to the *CTE* and the elastic modulus of the coating. The slope

upon cooling almost equal to the one upon heating is an indication that no irreversible changes of these macroscopic properties have been induced by the fast thermal treatment. The kinetics of structural evolution is probably slower than the total annealing time. What changes is the value of σ_f. After the thermal cycle, the film is found in a tensile state of stress. This underlines that σ_{res} relaxation has occurred, due to some local structure reorganization associated to defects diffusion at relatively low temperatures.

3.4. Thermal annealing of a-WO$_{3-x}$ coatings

Temperature induced effects on a-WO$_{3-x}$ films is investigated by vacuum annealing treatments performed between 570 K and 870 K. SEM cross section images of annealed a-WO$_{3-x}$ coatings are shown in Fig. 9. Up to 570 K no substantial morphological changes are visible. Starting from 670 K, instead, SEM analysis clearly shows a morphology modification. The compact nanostructured morphology of as-deposited a-WO$_{3-x}$ evolves into a featureless, more compact one. This can be related to the annealing driven structural reorganization process, which, in turn, suggests that around 670 K crystallization occurs. SEM cross section images also show a decrease by about 20% of film thickness starting from 670 K. The thickness, indeed, goes from 3.3 μm to $\approx$ 2.7 μm at 670 K. This, in turn, is associated with an increase of film mass density, that goes from the as-deposited value of 5.7 g cm^{-3} to $\approx$ 7 g cm^{-3} above 670 K.

Raman spectroscopy is exploited to better highlight the observed crystallization process. The obtained spectra are shown in Fig. 10. Up to 570 K, no remarkable differences of the spectrum with respect to the as-deposited case can be detected. This is in agreement with SEM analysis, which does not report a strong variation of the film structure and morphology. At 670 K, instead, several new peaks become visible. These peaks grow in correspondence of 133 cm^{-1}, 273 cm^{-1}, 715 cm^{-1} and 805 cm^{-1}, which correspond to the principal peaks of the crystalline γ monoclinic phase of WO$_3$ [45]. The observed peaks width, in particular the width of the peak at 715 cm^{-1}, suggests that, at this temperature a consistent amount of amorphous structure is still present: the crystallization process is not completed. At 870 K, instead, definitely sharper peaks are found. Moreover, the positions of these peaks are slightly shifted with respect to the ones of γ-WO$_3$. This can be attributed to different factors, such as internal stresses developed during annealing or stoichiometry defects. For the former case, as highlighted by stress evolution measurements of Fig. 8, the growth of a new crystalline phase in an amorphous matrix can lead to the development of a high internal state of stress associated to atoms diffusion, grains coalescence and growth. For the latter, EDXS analysis performed on annealed samples confirms a slight reduction of the O/W ratio for a-WO$_{3-x}$ from $\approx$ 2.95 down to 2.88. This could suggest that a small part of the total amount of O$_2$ is only trapped in the as deposited film and can desorb at relevant temperatures.

The observed crystallization affects the mechanical properties of the films, which are assessed by Brillouin analysis following the same procedure adopted for a-WO$_{3-x}$ samples. The obtained elastic moduli are summarized in Fig. 11. As expected, if annealing is performed at 570 K only a slight increase of material stiffness is observed. At 670 K, instead, when crystallization begins, $E = 101$ GPa, $G = 36$ GPa and $G/K = 0.24$, with a consequent increase by about 36% of E with respect to the as-deposited condition. In agreement with what we found in [23], these properties can be due to an amorphous matrix in which nanocrystals are embedded. Finally, when the γ monoclinic WO$_3$ phase is better defined at 870 K, a further increase of the moduli is detected (i.e. $E = 127$ GPa, $G = 50$ GPa and $G/K = 0.38$). These results are in accordance with what we observed in Fig. 8 concerning the total stress evolution. We determined the relaxation temperature
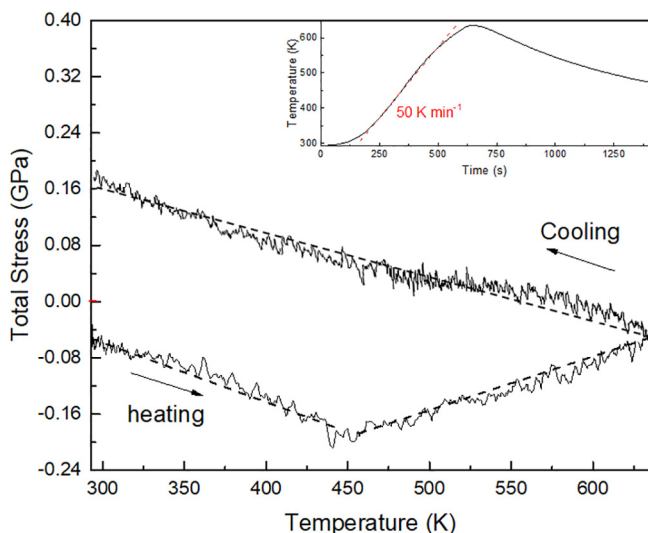
Fig. 8. Film stress evolution during annealing evaluated by the SC method. The black dotted line represents a linear fit of the mean value of the stress.
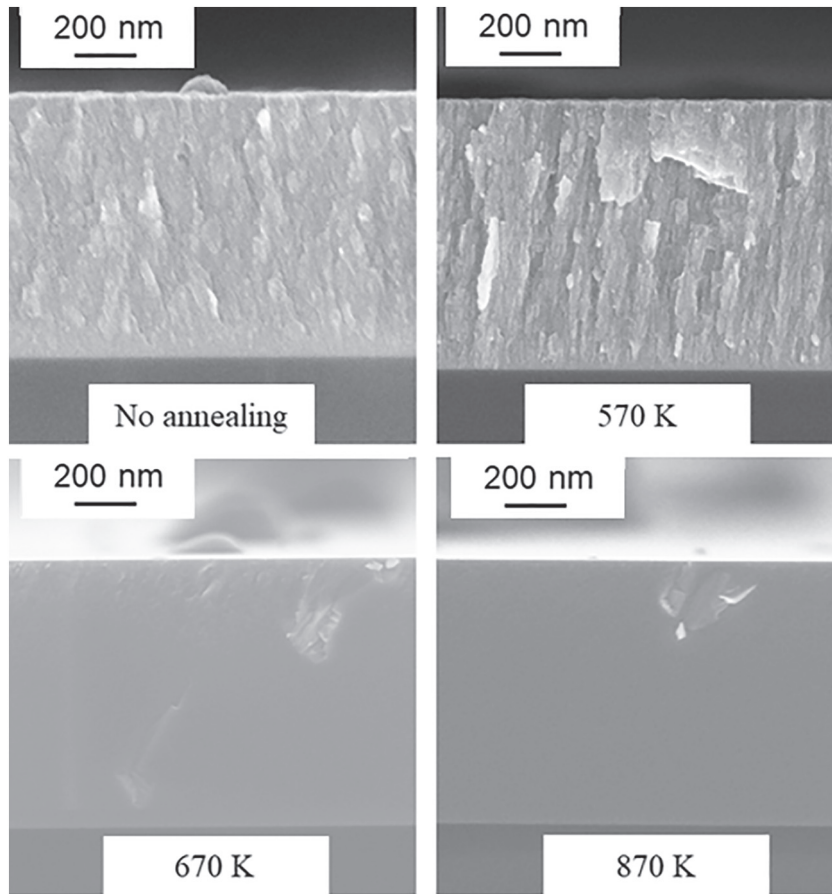
Fig. 9. SEM images of a-WO$_{3-x}$ samples annealed for 1 h in vacuum at different temperatures.

T_R to be at 450 K, and we found that even if we rapidly heat the sample at temperatures $T > T_R$ no changes of the macroscopic properties are observed. This agrees with the slight stiffening observed at 570 K. Consistently, only 1 h annealing treatments at 670 K can alter significantly the nanostructure and the properties of the material. The corresponding stiffening process is, in turn, attributed to different competitive processes, such as structural relaxation, free volume annihilation and short-range ordering (i.e. nano-crystals formation), which can increase the interatomic potential and consequently the elastic moduli of the material [46].
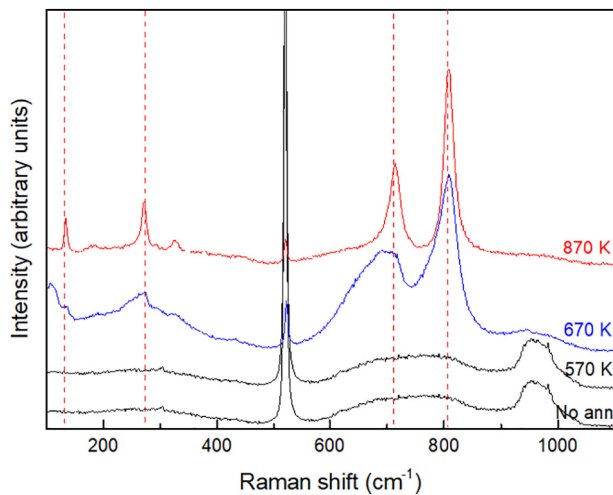

Fig. 10. Raman spectra of annealed a-WO$_{3-x}$ samples. The red dotted lines correspond to the principal peaks proper of γ monoclinic WO$_3$. Si substrate peaks are present at 521 cm^{-1} and at 960 cm^{-1}.
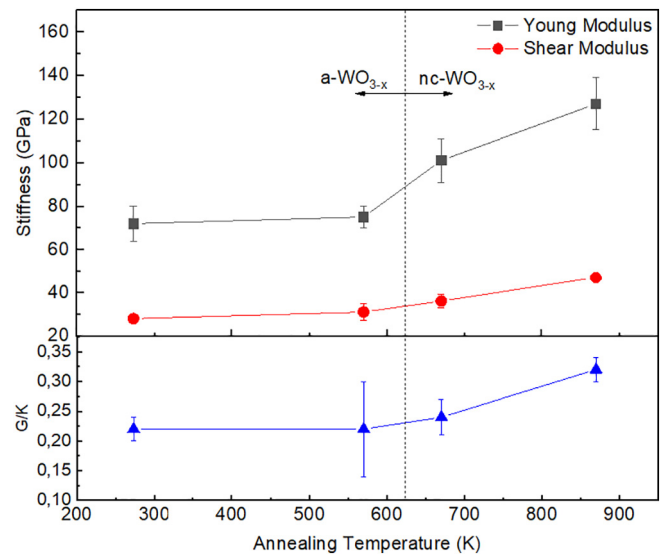

Fig. 11. Elastic moduli of annealed a-WO$_{3-x}$ films.

4. Conclusions

In this work we investigate the thermomechanical properties of different systems of amorphous tungsten-oxygen and tungsten-oxide coatings. Such properties are important for the design and construction of devices, in which the tungsten based layer is generally in contact with other layers, and in which the mechanical integrity is a crucial requirement. This is particularly critical when the films are required to operate at high temperatures or in the presence of external loads (e.g. thermophotovoltaic, solar cells, electronics). The samples were deposited by PLD, which allowed us to access a wide range of morphologies, structures and compositions of the films. We thus found the relationship between these properties and the thermomechanical ones. We explored a whole interval of properties, offering useful information to identify the type of coating which best fits each single application. The mechanical properties of the as-deposited films, namely the elastic moduli and the residual stress, resulted to be simultaneously influenced by the morphology and the O/W ratio: as the films become less dense and rich of oxygen, the stiffness and residual stresses linearly decrease. However, for ρ between 4.8 and 7 g cm^{-3} and O/W ratio between 2.6 and 3 the stiffness undergoes only small variations, consistently with a structure, revealed by XRD, which remains almost the same, while the electronic properties, revealed by resistivity and Raman measurements, have more significant variations. Among tungsten-oxide coatings, compact a-WO$_{3-x}$ films showed the most promising mechanical properties in the as deposited state, with a moderate stiffness, compressive residual stresses and a relatively high ability to locally allocate shear flow. These properties can be desired for applications under external thermal or mechanical loads. The quite high CTE and a quite low relaxation temperature must be considered for their use in high temperature applications. Crystallization into the monoclinic γ-WO$_3$ phase starts at 670 K, with a consequent strong crystallization induced stiffening and a decrease of local ductility. The lower observed relaxation temperature (i.e. 450 K) suggests that possible structural relaxation and diffusion processes already begin at temperatures well below the determined annealing temperature, without affecting the overall properties of the material. Since the knowledge of annealing kinetics can be crucial to determine the evolution of films properties under high temperatures, this type of analysis will require further investigation. Overall, the ensemble of our results can provide a guidance in the design of various devices which exploit tungsten based layers.

Data availability

The raw data required to reproduce these findings cannot be shared at this time due to technical or time limitations. The processed data required to reproduce these findings cannot be shared at this time due to technical or time limitations.

Acknowledgments

References

[1] H. Zheng, J.Z. Ou, M.S. Strano, R.B. Kaner, A. Mitchell, K. Kalantar-zadeh, Nanostructured tungsten oxide - properties, synthesis, and applications, Adv. Funct. Mater. 21 (2011) 2175–2196.

[2] S. Wang, W. Fan, Z. Liu, A. Yu, X. Jiang, Advances on tungsten oxide based photochromic materials: strategies to improve their photochromic properties, J. Mater. Chem. C 6 (2018) 191.

[3] C.G. Granqvist, Transparent conductive electrodes for electrochromic devices: a review, Appl. Phys. A 57 (1993) 19.

[4] O.R. Nunez, A.J. Moreno Tarango, N.R. Murphy, L.C. Phinney, K. Hossain, C.V. Ramana, Physical characterization of sputter-deposited amorphous tungsten oxynitride thin films, Thin Solid Films 596 (2015) 160–166.

[5] B. Abdel Samad, P.V. Ashrit, B. Abdel Samad, P.V. Ashrit, Optimization of mixed conductivity through nanostructure control in WO$_3$ thin films, Thin Solid Films 636 (2017) 717–722.

[6] A. Karuppasamy, A. Subrahmanyam, Studies on electrochromic smart windows based on titanium doped WO3 thin films, Thin Solid Films 516 (2007) 175–178.

[7] W. Li, P. Da, Y. Zhang, Y. Wang, X. Lin, X. Gong, G. Zheng, WO3 Nanoflakes for enhanced photoelectrochemical conversion, ACS Nano 8 (2014) 11770–11777.

[8] S. Shin, H. Soo Han, J.S. Kim, I.J. Park, M.H. Lee, K.S. Hong, I.S. Cho, A tree-like nanoporous WO3 photoanode with enhanced charge transport efficiency for photoelectrochemical water oxidation, J. Mater. Chem. A 3 (2015) 12920.

[9] S.K. Deb, Opportunities and challenges in science and technology of WO$_3$ for electrochromic and related applications, Sol. Energ. Mat. Sol. 92 (2008) 245.

[10] T. Kikuchi, J. Kawashima, S. Natsui, R.O. Suzuki, Fabrication of porous tungsten oxide via anodizing in an ammonium nitrate/ethylene glycol/water mixture for visible light-driven photocatalyst, Appl. Surf. Sci. 422 (2017) 130–137.

[11] A. Yamamoto, Y. Abe, M. Kawamura, K. Sasaki, Effects of oxygen gettering and target mode change in the formation process of reactively RF sputtered WOx thin films, Vacuum 66 (2002) 269–273.

[12] D. Dellasega, G. Merlo, C. Conti, C.E. Bottani, M. Passoni, Nanostructured and amorphous-like tungsten films grown by pulsed laser deposition, J. Appl. Phys. 112 (2012) 084328.

[13] D. Dellasega, S.M. Pietralunga, A. Pezzoli, V. Russo, L. Nasi, et al. Tungsten oxide nanowires grown on amorphous-like tungsten films, Nanotechnology 26 (2015) 365601.

[14] R. Seelaboyina, Tungsten oxide nanowire synthesis from amorphous-like tungsten films, Nanotechnology 27 (2016) 112502.

[15] G.A. Niklasson, C.G. Granqvist, Electrochromics for smart windows: thin films of tungsten oxide and nickel oxide, and devices based on these, J. Mater. Chem. 17 (2007) 127–156.

[16] D.K. Nandi, S.K. Sarkar, Atomic layer deposition of tungsten oxide for solar cell application, Energy Procedia 54 (2014) 782–788.

[17] J.L. Enriquez-Carrejo, M.A. Ramos, J. Mireles-Jr-Garcia, A. Hurtado-Macias, Nano-mechanical and structural study of WO$_3$ thin films, Thin Solid Films 606 (2016) 148–154.

[18] N.M.G. Parreira, N.J.M. Carvalho, A. Cavaleiro, Synthesis, structural and mechanical characterization of sputtered tungsten oxide coatings, Thin Solid Films 510 (2006) 191–196.

[19] M.M. Hasan, A.S.M.A. Haseeb, H.H. Masjuki, Structural and mechanical properties of nanostructured tungsten oxide thin films, Surf. Eng. 28 (10) (2012) 778–785.

[20] A. Pezzoli, D. Dellasega, V. Russo, A. Gallo, P.A. Zeijlmans van Emmichoven, M. Passoni, Thermal annealing and exposure to divertor-like deuterium plasma of tailored tungsten oxide coatings, J. Nucl Mater. 463 (2015) 1041–1044.

[21] A. Baserga, V. Russo, F. Di Fonzo, A. Bailini, D. Cattaneo, C.S. Casari, A. Li Bassi, C.E. Bottani, Nanostructured tungsten oxide with controlled properties: synthesis and Raman characterization, Thin Solid Films 515 (2007) 6465–6469.

[22] A. Bailini, F. Di Fonzo, M. Fusi, C.S. Casari, A. Li Bassi, V. Russo, A. Baserga, C.E. Bottani, Pulsed laser deposition of tungsten and tungsten oxide thin films with tailored structure at the nano- and mesoscale, Appl. Surf. Sci. 253 (2007) 8130–8135.

[23] E. Besozzi, D. Dellasega, A. Pezzoli, C. Conti, M. Passoni, M.G. Beghi, Amorphous, ultra-nano- and nano-crystalline tungsten-based coatings grown by Pulsed Laser Deposition: mechanical characterization by Surface Brillouin Spectroscopy, Mater. Des. 106 (2016) 14–21.

[24] D. Dellasega, V. Russo, A. Pezzoli, C. Conti, N. Lecis, E. Besozzi, M. Beghi, C.E. Bottani, M. Passoni, Boron films produced by high energy Pulsed Laser Deposition, Mater. Des. 134 (2017) 35–43.

[25] E. Besozzi, D. Dellasega, A. Pezzoli, A. Mantegazza, M. Passoni, M.G. Beghi, Coefficient of thermal expansion of nanostructured tungsten based coatings assessed by substrate curvature method, Mater. Des. 137 (2018) 192–203.

[26] F.G. Ferre, E. Bertarelli, A. Chiodoni, D. Carnelli, D. Gastaldi, P. Vena, M.G. Beghi, F. Di Fonzo, The mechanical properties of a nanocrystalline Al$_2$O$_3$/a-Al$_2$O$_3$ composite coating measured by nanoindentation and Brillouin spectroscopy, Acta Mater. 61 (2013) 2662–2670.

[27] T. Kundu, Mechanics of elastic waves and ultrasonic nondestructive evaluation, in: T. Kundu (Ed.), Ultrasonic Nondestructive Evaluation, CRC Press, Boca Raton, FL, 2004, Chapter 10.

[28] M. Beghi, F.D. Fonzo, S. Pietralunga, C. Ubaldi, C. Bottani, Precision and accuracy in film stiffness measurement by brillouin spectroscopy, Rev. Sci. Inst. 82 (2011) 053107.

[29] G. Stoney, The tension of metallic films deposited by electrolysis, Proc. R. Soc. Lond. Ser. A Contain. Pap. Math. Phys. Character 82 (553) (1909) 172–175.

[30] L. Berggren, G.A. Niklasson, Optical absorption and durability of sputtered amorphous tungsten oxide films, Solid State Ion. 165 (2003) 51–58.

[31] F. Di Fonzo, Synthesis and characterization of tungsten and tungsten oxide nanostructured films, Catal. Today 116 (1) (2006) 69–73.

[32] K. von Rottkay, M. Rubin, S.-J. Wen, Optical indices of electrochromic tungsten oxide, Thin Solid Films 306 (1997) 10–16.

[33] G.A. Niklasson, C.G. Granqvist, Electrochromics for smart windows: thin films of tungsten oxide and nickel oxide, and devices based on these, J. Mater. Chem. 17 (2007) 127–156.

[34] R. Daniel, K.J. Martinschitz, J. Keckes, C. Mitterer, The origin of stresses in magnetron-sputtered thin films with zone T structures, Acta Mater. 58 (2010) 2621–2633.

[35] L.B. Freund, Dynamic Fracture Mechanics,ISBN 978-0521629225. Cambridge University Press. 1998, 83.

[36] E. Washizu, A. Yamamoto, Y. Abe, M. Kawamura, K. Sasaki, Solid State Ion. 165 (2003) 175.

[37] X. Sun, Z. Liu, H. Cao, Effects of film density on electrochromic tungsten oxide thin films deposited by reactive dc-pulsed magnetron sputtering, J. Alloys Compd. 504S (2010) S418–S421.

[38] X. Liu, H.-Q. Fan, Electronic structure, elasticity, Debye temperature and anisotropy of cubic WO3 from first-principles calculation, R. Soc. Open Sci. 5 (2018) 171921.

[39] L. Liang, M. Li, F. Qin, Y. Wei, Temperature effect on elastic modulus of thin films and nanocrystals, Philos. Mag. 9 (8) (2013) 574–583.

[40] C.A. Schuh, T.C. Hufnagel, U. Ramamurty, Mechanical behavior of amorphous alloys, Acta Mater. 55 (2007) 4067–4109.

[41] T. Polcar, N.M.G. Parreira, A. Cavaleiro, Tungsten oxide with different oxygen contents: sliding properties, Vacuum 81 (2007) 1426–1429.

[42] R.C. Weast, CRC Handbook of Chemistry and Physics, CRC Press, Boca Raton, 1988.

[43] T. Tokunaga, T. Kawamoto, K. Tanaka, N. Nakamura, Y. Hayashi, K. Sasaki, K. Kuroda, T. Yamamoto, Growth and structure analysis of tungsten oxide nanorods using environmental TEM, Nanoscale Res. Lett. 7 (1) (2012) 85.

[44] T. Takamori, Thermal expansion characteristics of polycrystalline tungsten oxides, J. Am. Ceram. Soc. 47 (10) (1964) 534–535.

[45] S. Hayashi, et al. Phase transitions in gas-evaporated WO_3 microcrystals: a Raman study, J. Phys. Soc. Jpn. 61 (1992) 916.

[46] G. Ouyang, X.L. Li, X. Tan, G.W. Yang, Size-induced strain and stiffness of nanocrystals, Appl. Phys. Lett. 031904 (2006) 89.